



TECHNICAL ARTICLE

# Mechanical and Microstructural Properties of Autogenous Arc Welds of 2 GPa Strength Hot-Press-Forming Steel

Kwangsoo Kim, Hanji Park, Namhyun Kang, Sanghoon Kang, Minjung Kang, and Cheolhee Kim

Submitted: 3 November 2022 / Revised: 20 April 2023 / Accepted: 16 May 2023 / Published online: 15 June 2023

Currently, the strength of hot-press-forming steel has been increased to produce lightweight vehicles, and in this study, the first arc welding investigation on a 2.0 GPa-strength hot-press-forming steel was conducted. Hot-press-forming steel sheets with thicknesses of 1.1 mm were butt-welded by gas tungsten arc welding without a filler metal, with the heat input controlled in the range of 140–260 J/mm. The weld metal, coarse-grained heat-affected zone (HAZ), and fine-grained HAZ had martensitic microstructures. The softened zone was composed of an intercritical HAZ (with polygonal ferrite and martensite/bainite) and a subcritical HAZ (with tempered martensite). The intercritical HAZ was softened the most during welding and fractured during tensile testing. The strengths of the arc welds were in the range of 1141–1264 MPa, which were 57–63% strength of the base metal. The equiaxed austenite on martensite or ferrite matrix was developed at the intercritical HAZ of gas tungsten arc welds, therefore transforming into the coarse martensite during quenching. However, the intercritical HAZ of laser welds indicated acicular austenite transforming into the fine martensite due to its high cooling rate. The intercritical HAZ softening was revealed to originate from carbon diffusion during the martensite to austenite transformation, which is unavoidable in arc welding and should be considered in the design of a welded structure.

**Keywords** arc welding, heat-affected zone, hot-press-forming steel, microstructure, softening, strength

## 1. Introduction

Hot-press-forming (HPF) steel, also known as hot-forming steel or press-hardened steel, is a boron-alloyed high-strength steel with a full martensitic microstructure. Considering martensitic steels has limited formability, HPF steel sheets are supplied as low-strength pearlite structures and formed above the austenitization temperature. During forming, they are simultaneously quenched in a water-cooled die, causing an austenite-to-martensite transformation. HPF steels with a tensile strength of 1.5 GPa, represented by 22MnB<sub>5</sub> steel, have been successfully applied to automotive body components, such as pillars, bumper beams, and impact beams.

Moreover, recently steel mill companies have introduced higher-grade HPF steels in the market (Ref 1–3).

As welding is the main assembly process for HPF steel sheets, the weldability of 1.5 GPa-grade HPF steels has been evaluated for various welding processes. These include resistance spot welding of overlap joints (Ref 4–8); laser welding of overlap (Ref 9–12), butt (Ref 13, 14), and lap–fillet joints (Ref 15), and tailor-welded blanks (Ref 16–19); arc welding of butt (Ref 20–22) and lap–fillet joints (Ref 23); and friction stir welding of butt (Ref 24) and overlap joints (Ref 25).

However, the literature on welding higher-grade HPF steel sheets is limited compared with that on 1.5 GPa-grade HPF steels. Fahlstrom *et al.* (Ref 26) evaluated the laser weldability of 1.8 GPa and 1.9 GPa-tensile-strength steels. Kang and Kim (Ref 27) presented the effects of surface oxides during laser welding of 1.8 GPa HPF steel, and Shi *et al.* (Ref 28) demonstrated laser-welded patchwork blanks of 1.8 GPa HPF steel. Lu *et al.* (Ref 29) conducted the first study on the laser weldability of 2.0 GPa HPF steel, and the authors (Ref 30, 31) investigated in detail the heat-affected zone (HAZ) softening and joint strength of laser welds. More recently, laser welds of 1.5/2.0 GPa dissimilar-strength HPF steels were analyzed (Ref 32). However, within the authors' knowledge, thus far, only laser welding has been investigated for HPF steels above 1.8 GPa.

The HAZ of an HPF-steel-weldment is softened during welding, whereas that of a mild-steel-weldment is hardened owing to the high cooling rate during welding. For partial or full martensitic steels, the degree of HAZ softening increases with increasing the tensile strength of the base metal (Ref 13, 24, 33). In a previous study on 1.5 GPa-grade HPF steel (Ref 13), the tensile strength of a laser-welded specimen was reduced by 15% owing to HAZ softening, even by low-heat-input laser welding. As a relatively high input is applied to HPF steel during arc welding, a more severe loss in tensile strength is expected compared with laser welding.

**Kwangsoo Kim**, School of Materials Science and Engineering, Pusan National University, Busan 46241, Korea; and Production Support Team, DNV Korea, Busan 48120, Korea; **Hanji Park**, Department of Mechanical and Materials Engineering, Portland State University, Portland, OR 97201; and Advanced Materials Process Research Institute, Inha University, Incheon 22201, Korea; **Namhyun Kang**, School of Materials Science and Engineering, Pusan National University, Busan 46241, Korea; **Sanghoon Kang** and **Minjung Kang**, Advanced Joining & Additive Manufacturing R&D department, Korea Institute of Industrial Technology, Incheon 21999, Korea; and **Cheolhee Kim**, Department of Mechanical and Materials Engineering, Portland State University, Portland, OR 97201; and Advanced Joining & Additive Manufacturing R&D department, Korea Institute of Industrial Technology, Incheon 21999, Korea. Contact e-mails: nhkang@pusan.ac.kr and chkim@kitech.re.kr.

**Table 1 Chemical composition of base metal (wt.%)**

Docol® PHS CR 2000								
C	Si	Mn	P	S	Cr	B	Nb	Ti
0.346	0.25	1.20	0.011	0.001	0.14	0.0015	0.044	0.01

Along with resistance spot welding, arc welding is an important welding process in automotive body assembly. In this study, autogenous gas tungsten arc welding was conducted on a 2.0 GPa-grade HPF steel. The mechanical and metallurgical characteristics of the welds were investigated with various heat inputs per unit length. The measured properties were compared with those by laser welding with smaller heat input, and kinetics of HAZ softening was discussed based on the measured properties.

## 2. Experimental Setup

The base metal (BM) used was Docol® PHS CR 2000 supplied by SAAB AB (Ref 34), and its chemical composition is summarized in Table 1. After the HPF process, the BM had the tensile strength, hardness, and elongation of 2.08 GPa, 609 HV, and 3.36%, respectively, and had a full martensite microstructure. The details of the HPF processing and BM properties are available in the previous study (Ref 20).

Welding specimens were machined to a width of 150 mm, length of 150 mm, and thickness of 1.1 mm. Fig. 1 shows that the specimen configuration is a gapless butt joint, along which gas tungsten arc welding is conducted. A 2% thoriated tungsten rod with a diameter of 2.4 mm was used as the electrode according to the AWS A5.12 M/A5.12:2009 standard (specification for tungsten and tungsten–alloy electrodes for arc welding and cutting). The distance between the gas nozzle and the specimen was 5 mm, and the arc length was 3 mm. The work angle was 90° in the cross-sectional direction, and the travel angle was 10° inclined against the forward direction. Argon shielding gas (99.9%) was supplied at a flow rate of 15 L/min.

The welding power source was operated in the direct current electrode negative mode. Table 2 lists the detailed welding conditions adopted to change the heat input. The heat input was varied from 140 to 260 J/mm, and the welding speed was set at 5 and 10 mm/s.

The mechanical and metallurgical properties of welded specimens were measured. The specimens were polished and etched with 3% nital solution (3 mL HNO<sub>3</sub> and 100 mL ethanol). The etched transverse cross sections were imaged using stereo microscopy, light optical microscopy (LOM), and field-emission scanning electron microscopy (FESEM) to study their microstructures. In the metallurgical analysis, the laser welding specimens used in the authors' previous study (Ref 30) were compared with the arc welded specimens. In the comparative study, the laser power and welding speed were 2 kW and 7 m/min, respectively, and the heat input was 17.1 J/mm, much lower than that of gas tungsten arc welding in this study. Details of the laser welding conditions are provided in the previous study (Ref 30). To investigate the retained austenite in intercritical HAZ (ICHAZ), electron backscattered

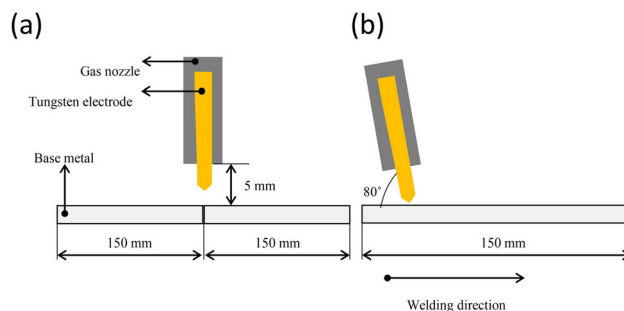


**Fig. 1** Welding joint configuration and arc welding torch arrangement: (a) transverse and (b) longitudinal directions

diffraction (EBSD) was performed at an acceleration voltage of 15 kV, a working distance of 15 mm, and a step size of 0.05  $\mu\text{m}$ .

Three tensile specimens per condition were extracted from the welded specimens by using electrical discharge machining. The gage width and length were 12.5 mm and 50 mm, respectively, and the detailed shape is specified in the ASTM E8 standard. Static tensile tests were conducted at a head speed of 1 mm/min. The micro-Vickers hardness distribution was measured along the specimen centerline of the cross section of each specimen. Hardness measurements were conducted for 81 measuring points at an indent interspacing of 0.22 mm, and the load and hold time were 1.96 N and 10 s, respectively.

## 3. Results and Discussion

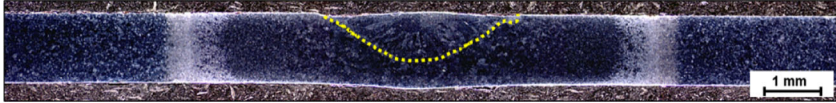
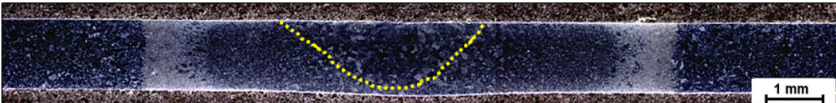


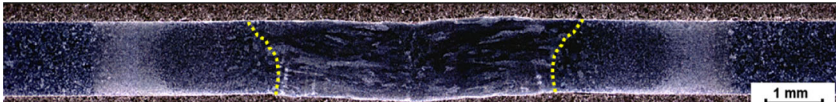
### 3.1 Macrosections and Hardness Profiles for Various Heat Inputs

Table 3 reports the macrosectional dimensions of the gas tungsten (GTA) welds produced for various heat inputs. Each fusion zone is indicated by a yellow dotted line. Noticeably, the bead width increased with increasing heat input. As the heat input was increased from 140 to 260 J/mm, the bead width in the centerline increased from 3.0 to 4.4 mm. White bands are observed on the cross sections outside the weld metal (WM), indicating the location of the ICHAZ (Ref 9, 13, 30). Fig. 2 shows that the hardness of the WM decreases with the increase in the heat input, and the Pearson's  $r$  value was  $-0.949$ . In contrast, the hardness of the supercritical HAZ adjacent to the WM was approximately 600 HV regardless of heat input and comparable to the BM hardness of 609 HV. The hardness of the ICHAZ with respect to the heat input shows a weak negative correlation with Pearson's  $r$  value ( $-0.374$ ). In addition, the distance between the ICHAZs increased from 6.2 to 9.2 mm on increasing the heat input from 140 to 260 J/mm.

**Table 2** Welding parameters and heat input per unit length

Specimen No.	Welding current, A	Welding voltage, V	Welding speed, mm/s	Heat input per unit length, J/mm
1	100	14	10	140
2	110	14.5	10	160
3	120	15	10	180
4	130	16	10	208
5	100	13	5	260

**Table 3** Macro-etched cross sections of welds with respect to heat input. Fusion lines are indicated by yellow dotted lines

Specimen No.	Heat input per unit length, J/mm	Cross section
1	140	
2	160	
3	180	
4	208	
5	260	

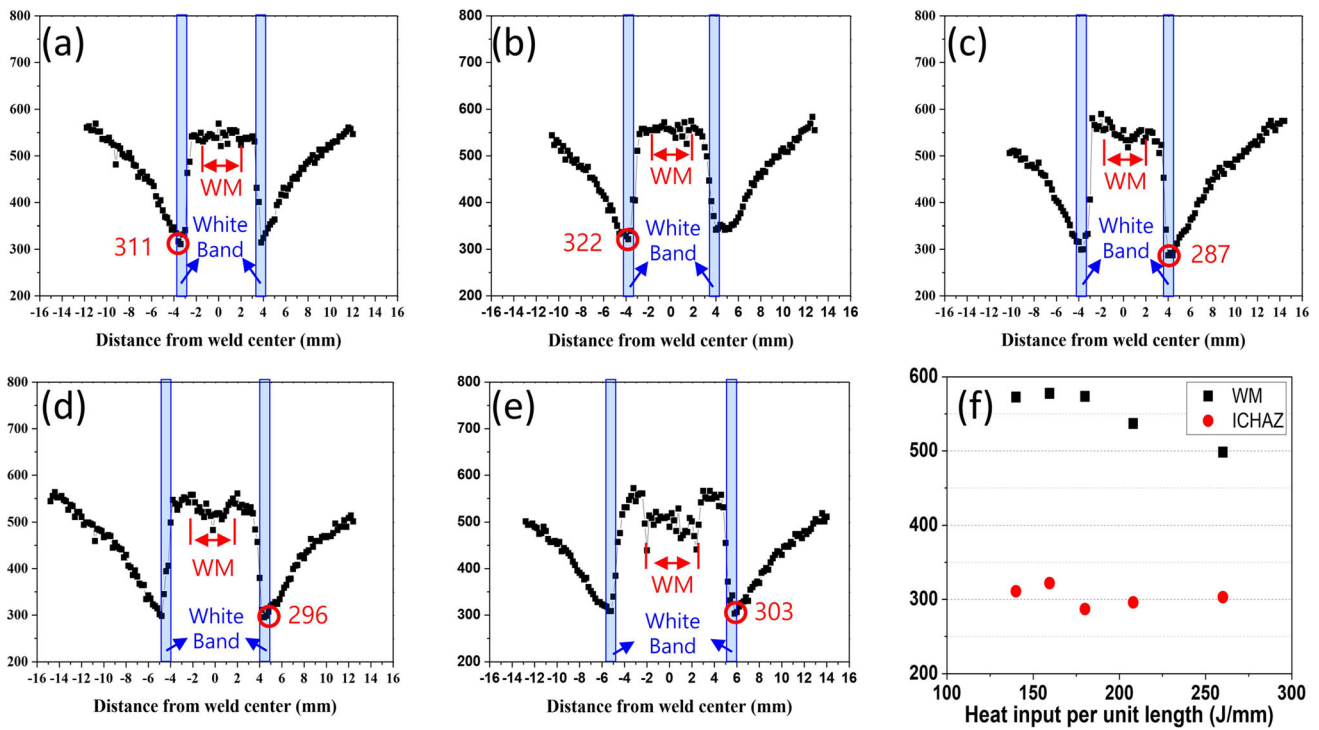
### 3.2 Mechanical Behavior for Various Locations

Fig. 3 shows the cross-sectional LOM images of typical welds, and the WM and the HAZ are noticeable. The detailed morphology of the welds was analyzed using FESEM, and the results are shown in Fig. 4. The BM had a full martensitic microstructure with a needle-like lath morphology (Fig. 3(b) and 4(a)). The ICHAZ exhibited a dual-phase structure of ferrite and martensite (Fig. 3(e), 4(d) and (e)), whereas other locations, such as the coarse-grained HAZ, fine-grained HAZ, subcritical HAZ, and BM, were composed of martensitic lath and/or tempered martensite.

No phase transformation is observed in the subcritical HAZ because the peak temperature is lower than the  $A_{C1}$  temperature; the tempered martensite (TM), including carbides,

precipitates primarily along the prior austenite grain (PAG) and lath boundaries. Owing to the tempering of martensite, the sharpness of the martensite lath was reduced, whereas the packet shape remained (Fig. 3(c) and (d)). Within the SCHAZ, the locations closer to the BM (subcritical HAZ1 in Fig. 3(c) and 4(b)) showed sharper martensitic laths and fewer tempered carbides than the locations closer to the ICHAZ (subcritical HAZ2 in Fig. 3(d) and 4(c)).

The ICHAZ presented polygonal grains in the LOM image (Fig. 3(e)); more specifically, it was comprised of polygonal ferrite (PF) and martensite (M) (Fig. 4(d) and 4(e)). The full martensite of the BM is transformed into polygonal ferrite and austenite at the peak temperature between the  $A_{C1}$  and  $A_{C3}$



**Fig. 2** Vickers hardness distributions according to heat input: (a) specimen 1, (b) specimen 2, (c) specimen 3, (d) specimen 4, and (e) specimen 5; (f) comparison of the hardness of weld metal and intercritical HAZ

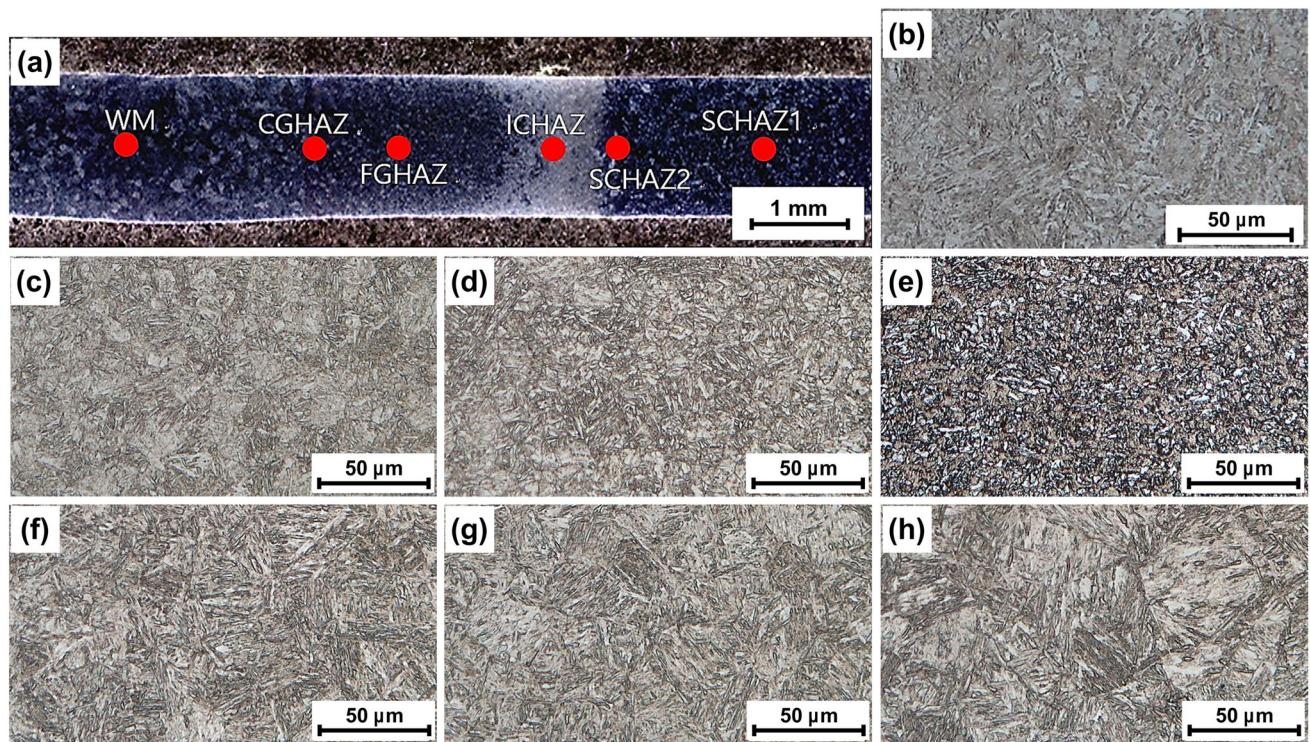


**Fig. 3** LOM images of welded specimen no. 2 for various locations: (a) a general view of transverse weld, (b) base metal, (c) subcritical HAZ1, (d) subcritical HAZ2, (e) intercritical HAZ, (f) fine-grained HAZ, (g) coarse-grained HAZ, and (h) weld metal

temperatures. Subsequently, the austenite is transformed into the nonequilibrium phase of martensite during cooling. Only the ICHAZ presents an equilibrium phase (polygonal ferrite), accompanied by martensite and bainite as nonequilibrium

phases. Therefore, the ICHAZ has a lower surface energy than the other zones (Ref 35) and has a relatively lower reaction with the etchant, resulting in the white bands at the cross sections, as seen in Table 3.

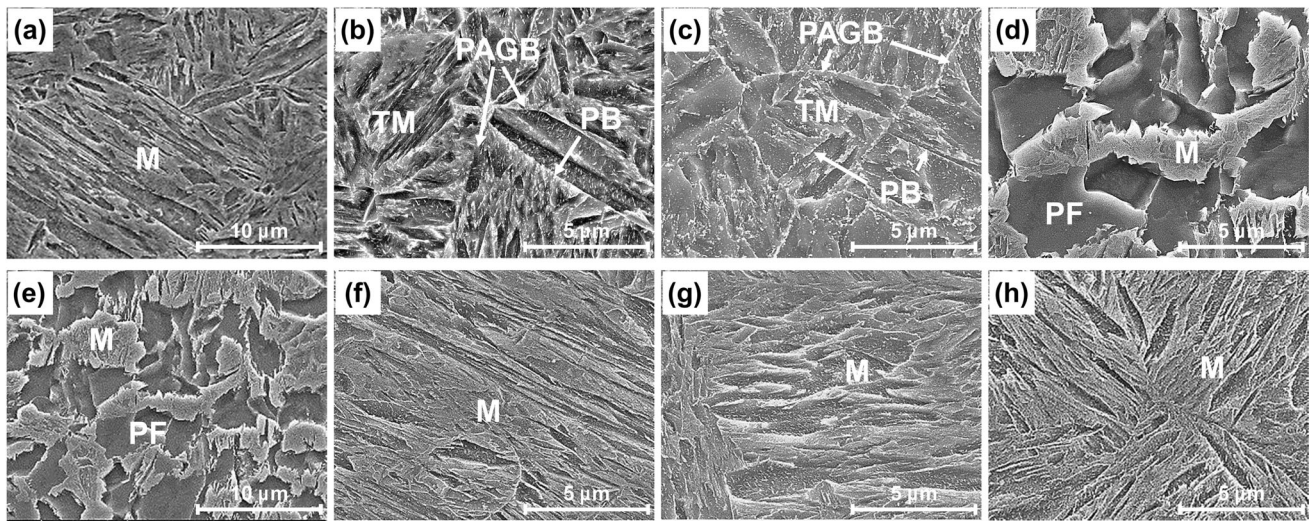


**Fig. 4** SEM images of welded specimen no. 2 for various locations: (a) base metal, (b) subcritical HAZ1, (c) subcritical HAZ2, (d) intercritical HAZ (x10,000), (e) intercritical HAZ (x5,000), (f) fine-grained HAZ, (g) coarse-grained HAZ, and (h) weld metal

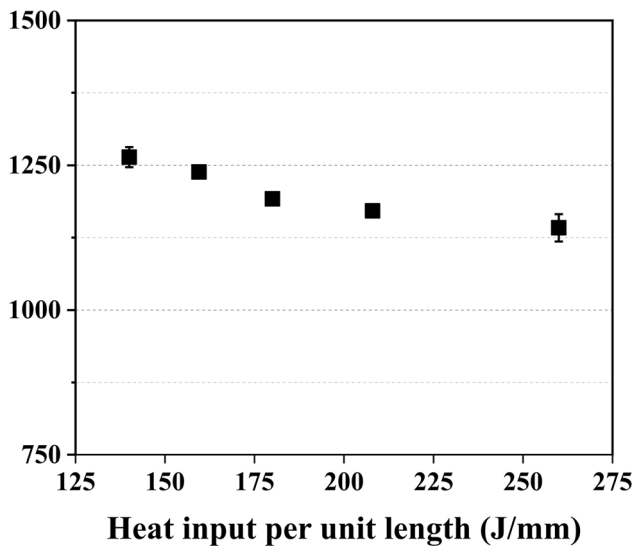


**Fig. 5** Tensile strengths of welds

As shown in Fig. 3(f)-(h) and 4(f)-(h), the fine-grained HAZ, coarse-grained HAZ, and WM regions became fully austenitic during heating and transform into full martensite during cooling owing to their peak temperatures higher than the  $A_{C3}$  temperature and the extremely high hardenability of the HPF steel, confirmed by the hardness profile shown in Fig. 2. In contrast, the ICHAZ and subcritical HAZ regions cannot reach the full austenization temperature ( $A_{C3}$ ) during heating, but transform into partial and tempered martensite, respectively, after welding. Consequently, the hardness values of the ICHAZ and the subcritical HAZ were relatively lower than that of the BM. The lowest hardness was observed in the ICHAZ, comprising a dual-phase structure of polygonal ferrite and martensite.

### 3.3 Tensile Strengths for Various Welds

The tensile strengths of the welds, as shown in Fig. 5, decreased linearly with increasing heat input. Fig. 6 shows the

fracture locations in the tensile testing, indicating that a tensile fracture occurs near the ICHAZ in all cases. This test was associated with the ICHAZ having the lowest hardness, as shown in the hardness profiles in Fig. 2.

The tensile strength presents better linearity (Fig. 5) with the heat input than the hardness (Fig. 2(f)) with respect to the heat input. Pearson's  $r$  value is  $-0.9568$ , much better than that between the heat input and the hardness ( $-0.374$ ). The relatively low linearity between the heat input and the hardness is caused by the spatial resolution of the hardness measurement in the ICHAZ. As shown in Fig. 2, because the ICHAZ is narrow, the hardness is measured at only one or two points within it.

A tensile fracture is initiated in the middle of the specimen, as shown in Fig. 6(a), and propagates toward the edges. Simultaneous crack initiation at multiple locations was confirmed by craters, marked as red arrows in the middle (Fig. 6(b)). Moreover, shear lips and slight necking were observed at the edges with mid-to-edge crack propagation (marked as white arrows in Fig. 6(b)). Therefore, the fracture surface with a cup-and-cone shape had a ductile mode fracture (Fig. 6(b)). A dimple fracture was confirmed in the more detailed surfaces of the fracture (Fig. 7).

### 3.4 Microstructural Features of Weld Metal and HAZ According to Heat Input

In this section, the microstructures of the WM and ICHAZ of GTA welds with higher heat inputs and laser welding with a much lower heat input of 17.1 J/mm are discussed. The WM, coarse-grained HAZ, and fine-grained HAZ showed fully martensitic microstructures because the peak temperature exceeded the  $A_{C3}$  temperature, whereas the peak temperature of the ICHAZ lay between the  $A_{C1}$  and  $A_{C3}$  temperatures. In particular, HAZ softening occurred in the ICHAZ and subcritical HAZ, and the softening kinetics are discussed in detail.

**3.4.1 Weld Metal Morphology for Various Heat Inputs and Laser Welds.** Figure 8 presents the microstructures of the WMs of laser welding with a heat input of 17.1 J/mm and GTA welding with varying heat inputs between 160 and 260 J/mm, which increment was approximately 50 J/mm. As the heat input increased in GTA welding, the WM was primarily martensitic and

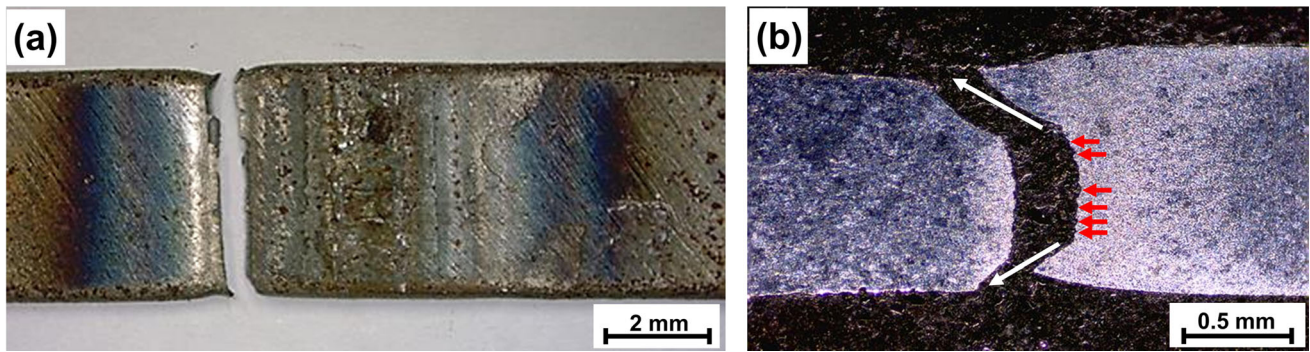


**Fig. 6** Fracture location of specimen 2 after tensile test: (a) top and (b) cross-sectional views (red arrows mark locations of fracture initiation and white arrows indicate direction of shear lips) (Color figure online)

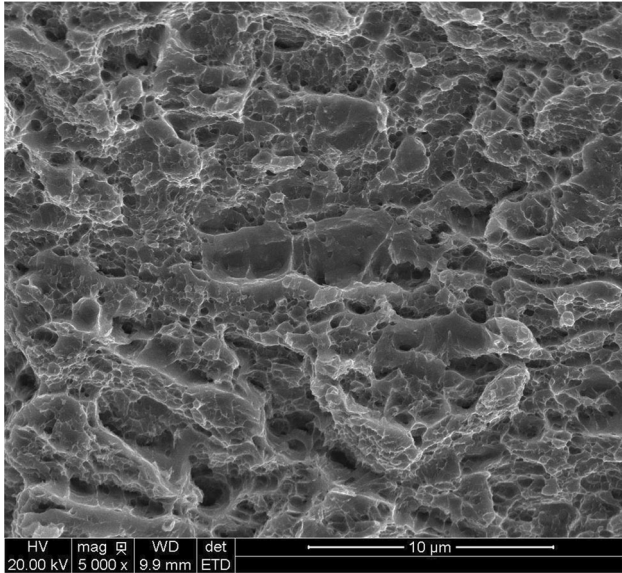


**Fig. 7** Fractograph of specimen 2

had a small amount of bainite-containing carbide precipitation (Fig. 8(d)). The decrease in the heat input increases the cooling rate, which decreases the time for carbon diffusion during the austenite-to-martensite transformation. At a magnification of  $\times 10,000$ , the lath width of the martensite decreased as the heat input decreased. The weakening of the martensite morphology was consistent with the decrease in the hardness with increasing the heat input. (Fig. 2). Finally, the WM morphologies of the laser and arc welds with the minimum heat input (specimen No. 2) were similar despite a significant difference in the heat input.

From the analytical solution for the temperature distribution of a thin sheet by a moving heat source (Ref 36), the cooling time from 800 °C to 500 °C can be calculated by the following equation (Ref 37):

$$T_{8/5} = \frac{(q/v)^2}{4\pi\lambda\rho cd^2} \left[ \frac{1}{(500 - T_0)^2} - \frac{1}{(800 - T_0)^2} \right] \quad (\text{Eq 1})$$

where  $q$  is the actual power of the heat source,  $v$  is the welding speed,  $\lambda$  is the thermal conductivity,  $\rho$  is the density,  $c$  is the specific heat,  $d$  is the thickness of the sheet, and  $T_0$  is the room temperature in degree Celsius. The actual power of the heat source can be calculated by multiplying the welding power and the welding efficiency,  $\eta$ .

The cooling rate for each case is calculated using the material properties and parameters listed in Table 4, and the

calculated values are listed in Table 5. The mill maker recommends a cooling rate of at least 60 K/s for the hot-press-forming process to achieve full design hardness (Fig. 9) (Ref 34). The cooling rates for Fig. 8(a) and (b) are higher than 60 K/s, explaining the identical WM morphology for both cases despite the large difference in the cooling rate. In the highest heat input case (260 J/mm), the cooling rate is reduced to 10.3 K/s. Therefore, bainite formation in Fig. 8(d) can be explained by the cooling rate and the continuous cooling transformation (CCT) diagram (Fig. 9).

**3.4.2 ICHAZ Morphology for Various Heat Inputs Arc Welds and Laser Welds.** In the welds of partial or full martensitic steel with a strength over 780 MPa, softening is unavoidable in the ICHAZ (Ref 39). Consequently, the width of the ICHAZ (Ref 40) and the amount of softening determine the strength of the welded joint and the fracture location during tensile testing (Ref 33).

The ICHAZ width was measured at five points along the depth direction for the laser welds and arc welding specimen no. 2, and it was indicated with the boxplot shown in Fig. 10. The ICHAZ width with GTA welding was 380  $\mu\text{m}$ , approximately 13 times larger than that in laser welding (29  $\mu\text{m}$ ). In both cases, the tensile specimens were fractured in the ICHAZ. In the laser welding of 800 MPa-grade dual-phase steel (Ref 40), HAZ softening did not affect the fracture location and tensile strength when the heat input was below 42 J/mm, despite the ICHAZ width in the reference being much larger than the ICHAZ width in this study. Furthermore, in the case of 1180 MPa-grade transformation-induced plasticity (TRIP) steel, the heat input criterion for determining the ICHAZ fracture was 80 J/mm (Ref 41). The ICHAZ hardness of 2.0 GPa-grade HPF steel was similar to that of 800 MPa-grade dual-phase steel and 1180 MPa-grade TRIP steel. However, BM fracture rarely occurred in this study despite the narrow ICHAZ because the strength difference between the ICHAZ and the BM was significantly larger than that of lower-grade steels.

Fig. 11 shows the ICHAZ microstructures for various heat inputs. Although the laser welds with a heat input of 17.1 J/mm and GTA welding specimen No. 2 with a heat input of 160 J/mm indicated similar WM microstructures of full martensite (Fig. 8), the ICHAZ microstructures were clearly different from each other (Fig. 11). The ICHAZs of the GTA welds consisted of polygonal ferrite and martensite, whereas those of the laser welds included martensite and lath ferrite. It was also coincided with the previous study (Ref 30). The WM microstructure

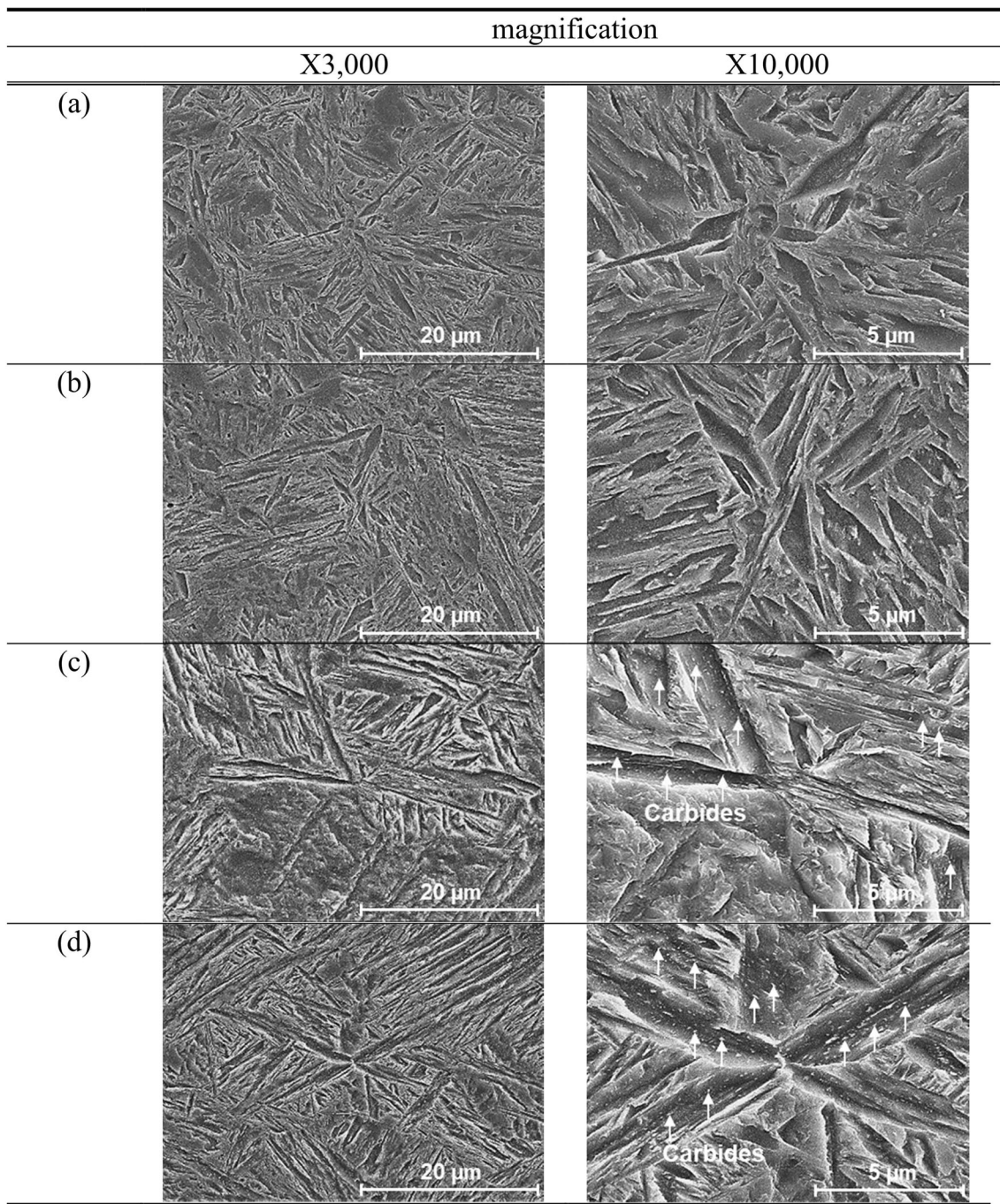


**Fig. 8** Microstructure of weld metal according to heat input: (a) 17.1 J/mm (laser weld), (b) 160 J/mm (specimen no. 2), (c) 208 J/mm (specimen no. 4), and (d) 260 J/mm (specimen no. 5)

**Table 4** Material properties and parameters for cooling rate calculation (Ref 38)

Parameter	Value
Welding efficiency, $\eta$	0.5
Thermal conductivity, $\lambda$ ( $\text{W}\cdot\text{m}^{-1}\cdot\text{K}^{-1}$ )	45
Density, $\rho$ ( $\text{kg}\cdot\text{m}^{-3}$ )	7200
Specific heat, $c$ ( $\text{J}\cdot\text{kg}^{-1}$ )	703.4
Thickness of sheet, $d$ (m)	0.0012
Room temperature, $T_0$ ( $^{\circ}\text{C}$ )	25

according to the heat input is determined solely by the cooling rate along the CCT curve (Fig. 9) since the WM is rapidly cooled through the austenite single-phase area from a liquid state. In comparison, the ICHAZ is rapidly cooled from the austenite and ferrite area between  $A_1$ - $A_3$  temperatures, and the ICHAZ microstructure depends on the cooling rate and time to stay in the  $A_1$ - $A_3$  region according to the heat input. In the HPF steel welds with significantly high hardenability, most austenite in the  $A_1$ - $A_3$  region is transformed to martensite during quenching. A small amount of carbide is observed in the ICHAZ of the GTA welds when the cooling rate is 40 K/s or less (Fig. 9).

**Table 5** Cooling rates calculated for various heat inputs

Specimen	Heat input per unit length, J/mm	$T_{8/5}$ , s	Cooling rate, K/s
Laser	17.1	0.049	6100
Arc No.2	160	4.27	70.3
Arc No. 4	208	7.26	41.3
Arc No. 5	260	29.03	10.3

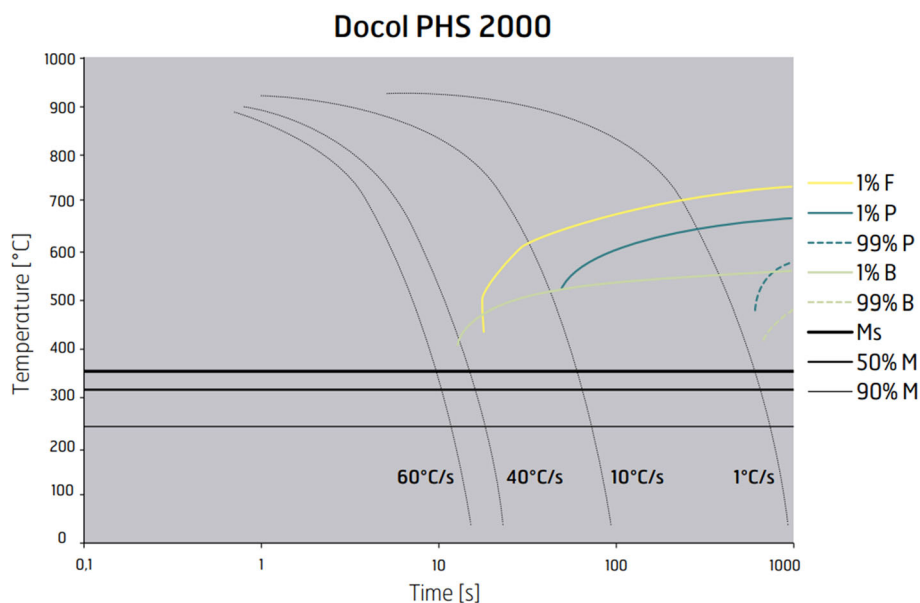


**Fig. 9** Continuous cooling transformation curves of Docol® PHS 2000 (Ref 34). Reprinted with permission from SSAB. Accessed at <https://www.ssab.com/en/brands-and-products/docol/automotive-steel-grades/press-hardening-steel>

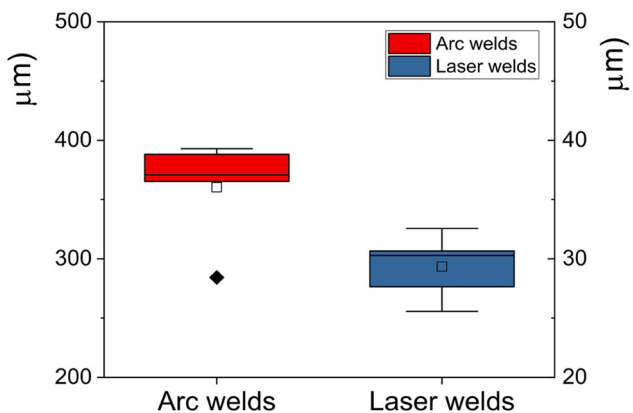


**Fig. 10** Box plots of intercritical HAZ widths measured at five locations. The heat inputs for arc and laser welds are 160 J/mm and 17.1 mm, respectively

The ICHAZ microstructure changes with the heat input significantly depending on the phase transformation process from martensite to ferrite and austenite. The microstructure of the ferrite–martensite transformation in the ICHAZ is completely different from that of martensite in the BM, suggesting that sufficient carbon is diffused and the grains are restructured during the martensite to austenite transformation in the ICHAZ. The kinetics of this process will be discussed in the coming Section 3.4.3.

HAZ softening is related to the welding process and specifically heat input and the cooling rate determines the extent of softening (Ref 42). The ICHAZs under various heat inputs are compared in Fig. 12, and the heat input for the samples is listed in Table 6. When heat input was between 17.1–45 J/mm, the boundary of the initial martensite morphology appeared to be maintained (Fig. 12(a)–(c)). As the heat input increased to 60–5.7 J/mm, the size of ferrite grain increased and the shape changed from lath into polygonal (Fig. 12(d) and (e)). By increasing the heat input more than 160 J/mm, the ferrite grain had the equiaxed morphology and the ferrite fraction increased (Fig. 12(f)).

**3.4.3 Kinetics of HAZ Softening for Gas Tungsten Arc and Laser Welds.** Apple and Krauss suggested two mechanisms in the martensite to austenite transformation of high carbon steel (Ref 43). At higher heating rate, plate-like or acicular austenite was alternated with martensite in the ICHAZ. At lower heating rate, austenite had equiaxed morphology, curved boundaries, and lack of sharp surface due to the thermally activated mechanism.

The kinetics for ICHAZ softening is depicted in Fig. 13. At the earliest stage of GTA welding, carbon in martensite is precipitated along the packet, block, and lath boundaries and their triple junctions in Fig. 13(a). As the temperature increased just below the  $A_{C1}$  temperature, carbide increased. Furthermore, the lath boundary got disappeared and the packet boundary became slightly curved, as shown in the Subcritical HAZ2 (Fig. 4(c)). At the ICHAZ, the temperature was between  $A_{C1}$  and  $A_{C3}$ , and carbon was diffused into austenite across the



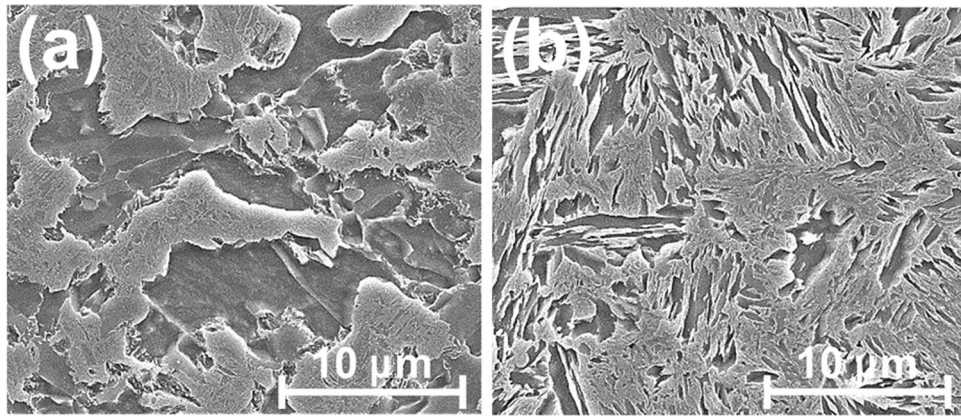


**Fig. 11** SEM images at different locations. Heat input per unit length was (a) 160 J/mm for arc welds and (b) 17.1 J/mm for laser welds

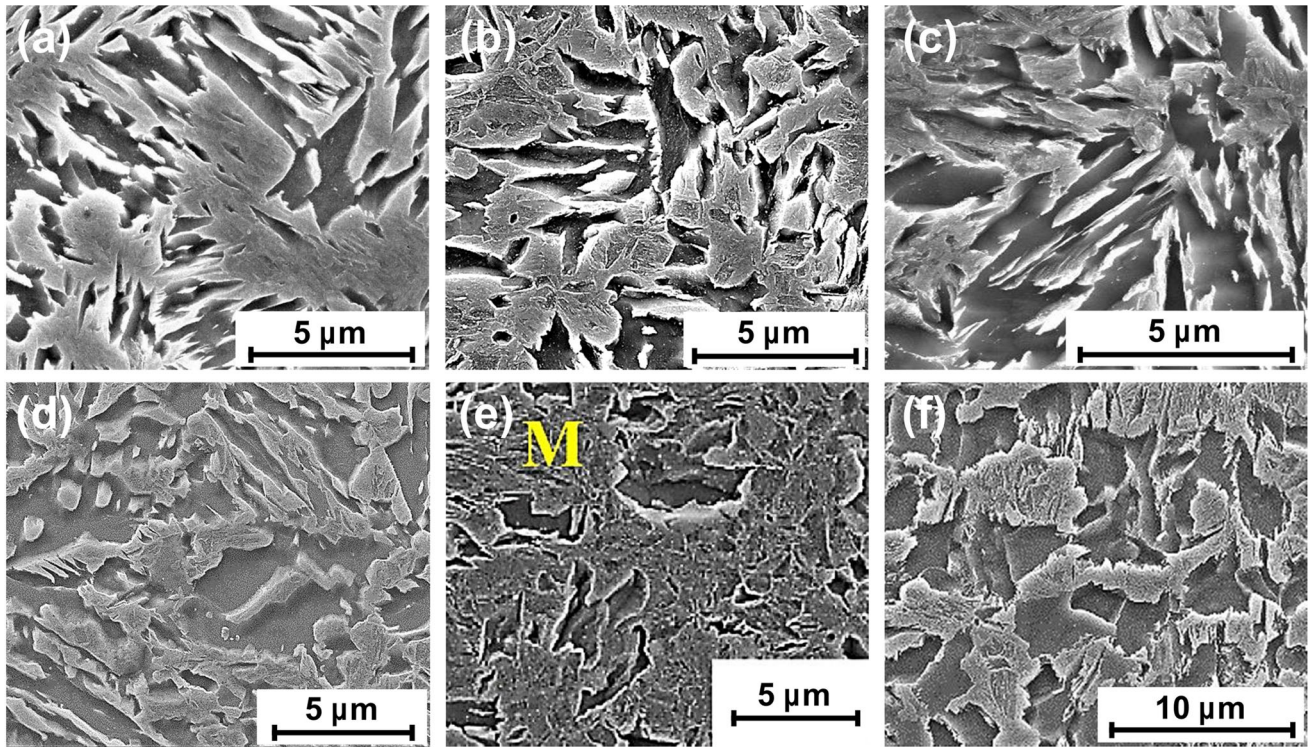


**Fig. 12** SEM images of intercritical HAZ of hot press forming steels from the previous studies (Ref 13, 27, 29-31). Panel (a) reproduced from Ref 35 under the CC BY license. Panel (b) reprinted with permission from M. Kang, C. Kim, Influence of surface oxide on mechanical properties of laser-welded hot-press-forming steel with strength of 1.8 GPa, *J. Laser Appl.*, 2018, 30(3), p 032415. Copyright 2018, Laser Institute of America. Panel (c) reprinted with permission from K. Kim, N. Kang, M. Kang et al., Effect of laser beam wobbling on the overlap joint strength of hot-press-forming steel over 2.0 GPa tensile strength, *J. Laser Appl.*, 2022, 34(1), p 012012. Copyright 2022, Laser Institute of America. Panel (d) reprinted with permission from C.-H. Kim, J.-K. Choi, M.-J. Kang et al., A study on the CO<sub>2</sub> laser welding characteristics of high strength steel up to 1500 MPa for automotive application, *Journal of Achievements in Materials and Manufacturing Engineering*, 2010, 39(1), p 79-86. Panel (e) reprinted from *Journal of Materials Research and Technology*, Vol 9, Li Lu, Zhenxin Liang, Jia Yang, Qian Sun, Tiancai Zhu, Xiaonan Wang, Investigation on laser welding of a novel hot-stamped steel with 2000 MPa, Pages 13147-13152, Copyright 2020, with permission from Elsevier. Panel (f) from Fig. 11(a)

boundaries. Due to the volume change during austenization (Ref 44), boundaries became round, and equiaxed austenite on martensite or ferrite matrix was developed at the ICHAZ. During cooling, the equiaxed austenite was transformed into coarse martensite (Fig. 13(a)). Therefore, the ICHAZ was composed of martensite, bainite, and ferrite as shown in Fig. 11(a).

In laser welding, phase transformation is relatively simple. The martensite boundaries of the packet, block, and lath were maintained during welding due to its high cooling rate. Carbon was diffused along the boundaries as in the GTA welding, and carbon-rich lath was transformed into austenite with sluggish diffusion of carbon across the boundaries. And a ferrite lath was formed in the area with relatively low carbon. During cooling,

**Table 6 Process parameters for samples in Fig. 12**

No	(a)	(b)	(c)	(d)	(e)	(f)
Process	Fiber laser	Disk laser	Fiber laser	Disk laser	Fiber laser	Gas tungsten arc
BM, GPa	2	1.8	2	1.5	2	1.5
Heat input, J/mm	17.1	36	45	60	85.7	160
Ref.	(Ref 30)	(Ref 27)	(Ref 31)	(Ref 13)	(Ref 29)	Fig. 11(a)

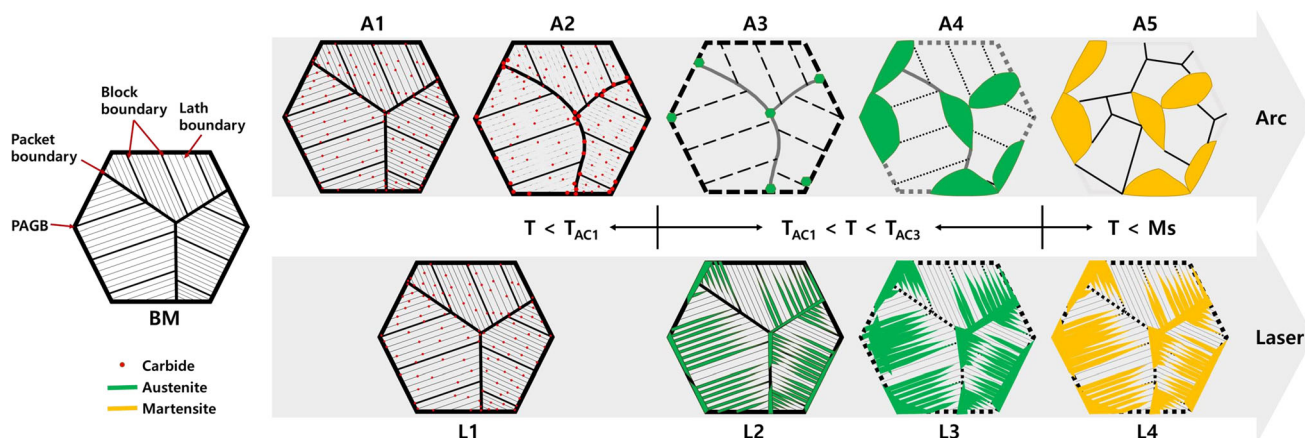


**Fig. 13** Schematic of the phase transformation process of intercritical HAZ in (a) gas tungsten arc and (b) laser welds

acicular austenite was transformed into fine martensite (Fig. 13(b)).

The phase distribution and retained austenite locations were confirmed by EBSD of GTA and laser welds (Fig. 14). In the phase map (Fig. 14(c) and (f)), the red grains represent the retained austenite with FCC structure (white arrows in Fig. 14), and the green color indicates either ferrite with the BCC structure or martensite with the BCT structure. The retained austenite was observed in the triple junction due to the high surface energy in both ICHAZs of GTA and laser welds. In image quality maps (Fig. 14(a) and (d)), the dark area represents martensite with high deformation density inside the grain. The martensite packets with various crystal orientations are represented as various colors in inverse-pole figure maps (Fig. 14(b) and (e)). The feature morphology of the ferrite and martensite packet corresponded well with Fig. 11.

## 4. Conclusions

This study conducted the first investigation on an arc-welded HPF steel with a strength of 2.0 GPa. A detailed analysis of the mechanical and microstructural properties of the autogenous GTA welds produced by various heat inputs (140-260 J/mm) was performed and the following conclusions were drawn:

1. In the GTA welds, the WM, coarse-grained HAZ, and fine-grained HAZ had fully martensite microstructures,

while the ICHAZ and subcritical HAZ contained dual-phase (ferrite and martensite) and tempered martensite, respectively. The ICHAZ had the lowest hardness among the weldments, ranging between 287 HV and 322 HV under the heat inputs applied in this study.

2. The tensile strength of the GTA welds decreased from 1264 to 1141 MPa as the heat input increased from 140 to 260 J/mm. Fracture occurred in the ICHAZ, the most softened zone, and it was initiated in the ductile mode at the mid-thickness of the specimen and propagated toward the edge.
3. The hardness of the coarse-grained HAZ and fine-grained HAZ was similar to that of the BM, while the WM had a slightly lower hardness than the BM. The WM primarily had a martensite structure, and a small amount of bainite formation was observed as the heat input was more than 200 J/mm, as confirmed by the CCT diagram.
4. The ICHAZ of GTA welds showed a dual-phase structure of polygonal ferrite and martensite/bainite, unlike those of the laser welds composed of martensite and lath ferrite. The width of the arc ICHAZ (380  $\mu\text{m}$ ) was significantly larger than that of the laser ICHAZ (29  $\mu\text{m}$ ).
5. The packet boundaries of ICHAZ of GTA welds became round and equiaxed austenite on martensite or ferrite matrix was developed at the ICHAZ, therefore transforming into the coarse martensite during quenching. However, the ICHAZ of laser welds indicated acicular austenite transforming into the fine martensite due to its high cooling rate.

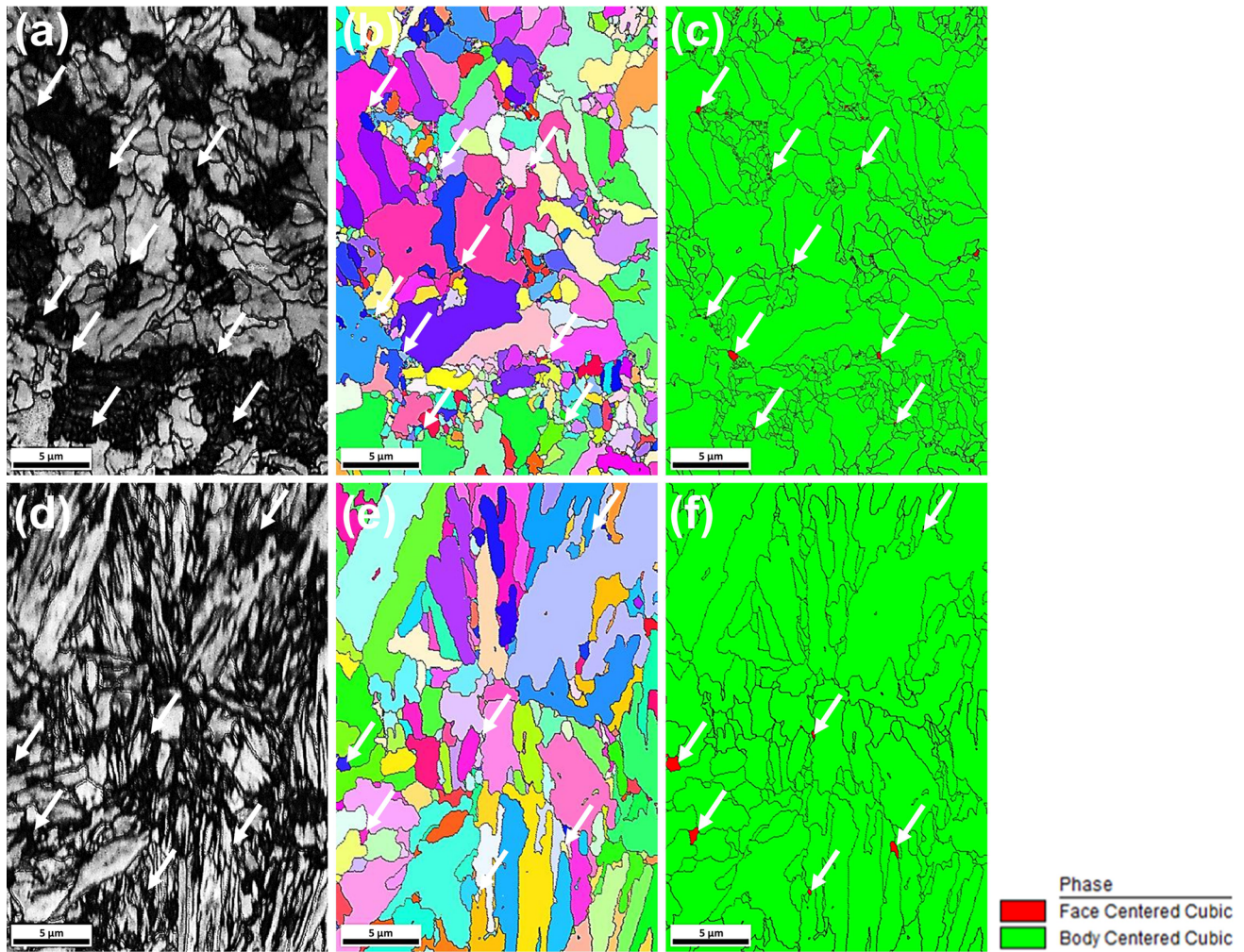


**Fig. 14** EBSD images of intercritical HAZ in (a)–(c) gas tungsten arc, (d)–(f) laser welds.

## Acknowledgments

This study was supported by the Technology Innovation Program-Materials and Components Development Program (Grant No. 20011427) and Industrial Strategic Technology Development Program (Grant No. 20014820), funded by the Korean Ministry of Trade, Industry, and Energy (MOTIE).

## Conflict of interest

The authors declare that they have no conflict of interest.

## References

1. H. Karbasian and A.E. Tekkaya, A Review on Hot Stamping, *J. Mater. Process. Technol.*, 2010, **210**(15), p 2103–2118
2. K.-G. Chin, C.-Y. Kang, J. Park et al., Fabrication of Hadfield-Cored Multi-Layer Steel Sheet by Roll-Bonding with 1.8-GPa-Strength-Grade Hot-Press-Forming Steel, *Met. Mater. Int.*, 2018, **24**(3), p 489–495
3. S.-M. Yun, H. Gwon, J. Oh et al., Suppression of Coating Layer Crack by Diffusion Heat Treatment in Al-Si Coated HPF Steels, *Met. Mater. Int.*, 2022, **28**, p 2668–2676
4. M.J. Kang and C.H. Kim, Analysis of Laser and Resistance Spot Weldments on Press-Hardened Steel, *Mater. Sci. Forum*, 2011, **695**, p 202–205
5. H. Fujimoto, M. Yasuyama, H. Ueda et al., Static Strength of Hot-Stamped Spot Welded Joints: Study on Spot Welding Tailored Blank Technology, *Weld. Int.*, 2017, **31**(9), p 681–691
6. R. Chen, C. Zhang, M. Lou et al., Effect of Al-Si Coating on Weldability of Press-Hardened Steels, *J. Mater. Eng. Perform.*, 2020, **29**(1), p 626–636
7. B.V. Feujofack Kemda, N. Barka, M. Jahazi et al., Modeling of Phase Transformation Kinetics in Resistance Spot Welding and Investigation of Effect of Post Weld Heat Treatment on Weld Microstructure, *Met. Mater. Int.*, 2021, **27**(5), p 1205–1223
8. H. You and C. Kim, Machine Learning Modeling and Hyper-Parameter Optimization for Weld Nugget Formation and Failure Behavior of Resistance Spot Welds, *J. Weld. Join.*, 2021, **39**(6), p 658–665
9. C. Kim, M. Kang, and Y. Park, Laser Welding of Al-Si Coated Hot Stamping Steel, *Proc. Eng.*, 2011, **10**, p 2226–2231
10. H. You, M. Kang, S. Yi et al., Modeling of Laser Welds Using Machine Learning Algorithm Part II: Geometry and Mechanical Behaviors of Laser Overlap Welded High Strength Steel Sheets, *J. Weld. Join.*, 2021, **39**(1), p 36–44
11. D. Zhang, Y. Qin, F. Zhao et al., Microstructure and Mechanical Properties of Laser Welded Al-Si Coated 22MnB<sub>5</sub> Hot Stamping Steel and Galvanized Steel, *J. Mater. Eng. Perform.*, 2021, **31**(2), p 1346–1357
12. F. Zhao, Y. Qin, D. Zhang et al., Effect of Filler Wire on Laser Lap Welding of Al-Si Coated 22MnB<sub>5</sub> Hot Stamping Steel, *J. Mater. Eng. Perform.*, 2022, **12**, p 9670–9680
13. C.-H. Kim, J.-K. Choi, M.-J. Kang et al., A Study on the CO<sub>2</sub> Laser Welding Characteristics of High Strength Steel Up to 1500 MPa for

- Automotive Application, *J. Achiev. Mater. Manuf. Eng.*, 2010, **39**(1), p 79–86
14. W. Xu, S. Yang, W. Tao et al., Effect of Al-Si Coating Removal State on Microstructure and Mechanical Properties of Laser Welded 22MnB<sub>5</sub> Steel, *J. Mater. Eng. Perform.*, 2022, **154**, p 108344
  15. M. Kang, C. Kim, and J. Lee, Weld Strength of Laser-Welded Hot-Press-Forming Steel, *J. Laser Appl.*, 2012, **24**(2), p 022004
  16. Y.-G. An, C.-Y. Kang, Y.-S. Kim et al., Microstructures and Hardness of DISK Laser Welds in Al-Si Coated Boron Steel and Zn Coated DP Steel, *J. Weld. Join.*, 2011, **29**(1), p 90–98
  17. M. Kang and C. Kim, Laser Welding for Hot-Stamped Tailor-Welded Blanks with High-Strength Steel/High-Energy Absorption Steel, *J. Laser Appl.*, 2014, **26**(3), p 032007
  18. M. Kang, C. Kim, and S. Bae, Laser Tailor-Welded Blanks for Hot-Press-Forming Steel with Arc Pretreatment, *Int. J. Automot. Technol.*, 2015, **16**(2), p 279–283
  19. M. Kang, Y.-M. Kim, and C. Kim, Effect of Heating Parameters on Laser Welded Tailored Blanks of Hot Press Forming Steel, *J. Mater. Process. Technol.*, 2016, **228**, p 137–144
  20. P. Russo Spena, F. D’Aiuto, P. Matteis et al., Dissimilar Arc Welding of Advanced High-Strength Car-Body Steel Sheets, *J. Mater. Eng. Perform.*, 2014, **23**(11), p 3949–3956
  21. G.K. Ahiale and Y.-J. Oh, Microstructure and Fatigue Performance of Butt-Welded Joints in Advanced High-Strength Steels, *Mater. Sci. Eng. A*, 2014, **597**, p 342–348
  22. T. Pfeifer and M.S. Węglowski, Characteristic of MAG Welded Joints of 22MnB<sub>5</sub> Steel Grade For Automotive Industry, *Adv. Manuf. Sci. Technol.*, 2014, **38**(4), p 71–80
  23. M. Kuo, Gas Metal Arc Welding of Advanced High Strength Steels, Great Design in Steel (GDIS) 2019ed., AUTO/STEEL Partnership, (2019)
  24. H. You, M. Kang, S. Yi et al., Comprehensive Analysis of the Microstructure and Mechanical Properties of Friction-Stir-Welded Low-Carbon High-Strength Steels with Tensile Strengths Ranging from 590 MPa to 1.5 GPa, *Appl. Sci.*, 2021, **11**(12), p 5728
  25. M. Kang, J. Yoon, and C. Kim, Hook Formation and Joint Strength in Friction Stir Spot Welding of Al alloy and Al-Si-Coated Hot-Press Forming Steel, *Int. J. Adv. Manuf. Technol.*, 2020, **106**(5–6), p 1671–1681
  26. K. Fahlström, K.-A. Persson, J.K. Larsson et al., Evaluation of Laser Weldability of 1800 and 1900 MPa Boron Steels, *J. Laser Appl.*, 2016, **28**(2), p 022426
  27. M. Kang and C. Kim, Influence of Surface Oxide on Mechanical Properties of Laser-Welded Hot-Press-Forming Steel with Strength of 1.8 GPa, *J. Laser Appl.*, 2018, **30**(3), p 032415
  28. D. Shi, K. Watanabe, J. Naito et al., Design Optimization and Application of Hot-Stamped B Pillar with Local Patchwork Blanks, *Thin-Walled Struct.*, 2022, **170**, p 108523
  29. L. Lu, Z. Liang, J. Yang et al., Investigation on Laser Welding of a Novel Hot-Stamped Steel with 2000 MPa, *J. Mater. Res. Technol.*, 2020, **9**(6), p 13147–13152
  30. K. Kim, N. Kang, M. Kang et al., Assessment of Heat-Affected Zone Softening of Hot-Press-Formed Steel over 2.0 GPa Tensile Strength with Bead-On-Plate Laser Welding, *Appl. Sci.*, 2021, **11**(13), p 5774
  31. K. Kim, N. Kang, M. Kang et al., Effect of Laser Beam Wobbling on the Overlap Joint Strength of Hot-Press-Forming Steel Over 2.0 GPa Tensile Strength, *J. Laser Appl.*, 2022, **34**(1), p 012012
  32. Z. Zhang, X. Wang, Q. Sun et al., Study on Microstructure and Properties of Laser Dissimilar Welded Joints of Ultra-High Strength PHS1500/PHS2000 Steel, *Opt. Laser Technol.*, 2022, **150**, p 107933
  33. M. Kang, I.-H. Jeon, H. Han et al., Tensile–Shear Fracture Behavior Prediction of High-Strength Steel Laser Overlap Welds, *Metals*, 2018, **8**(5), p 365
  34. Press Hardening Steels (PHS) for Complex Shapes, <https://www.ssab.com/en/brands-and-products/docol/automotive-steel-grades/press-hardening-steel>
  35. T. Hanamura, F. Yin, and K. Nagai, Ductile-Brittle Transition Temperature of Ultrafine Ferrite/Cementite Microstructure in a Low Carbon Steel Controlled by Effective Grain Size, *ISIJ Int.*, 2004, **44**(3), p 610–617
  36. D. Rosenthal, The Theory of Moving Sources of Heat and its Application of Metal Treatments, *Trans. ASME*, 1946, **68**, p 849–866
  37. K. Easterling, *Introduction to the Physical Metallurgy of Welding*, 2nd ed. Butterworth-Heinemann, Oxford, 1992
  38. C.H. Kim, W. Zhang, and T. DebRoy, Modeling of Temperature Field and Solidified Surface Profile during Gas–Metal Arc Fillet Welding, *J. Appl. Phys.*, 2003, **94**(4), p 2667–2679
  39. J.-K. Choi, M.-J. Kang, J.-H. Cho et al., Laser Welding Characteristics of Ultra High Strength Steel for Automotive Application, *J. Weld. Join.*, 2009, **27**(5), p 1–4
  40. X.-N. Wang, Q. Sun, Z. Zheng et al., Microstructure and Fracture Behavior of Laser Welded Joints of DP Steels with Different Heat Inputs, *Mater. Sci. Eng. A*, 2017, **699**, p 18–25
  41. S. Nam, H.W. Lee, C. Kim et al., Effects of High-Power Laser Heat Input on the Mechanical Properties of GPa-Grade Advanced High Strength TRIP Steel, *J. Weld. Join.*, 2021, **39**(5), p 505–512
  42. M. Xia, E. Biro, Z. Tian et al., Effects of Heat Input and Martensite on HAZ Softening in Laser Welding of Dual Phase Steels, *ISIJ Int.*, 2008, **48**(6), p 809–814
  43. C.A. Apple and G. Krauss, The Effect of Heating Rate on the Martensite to Austenite Transformation in Fe-Ni-C Alloys, *Acta Metall.*, 1972, **20**(7), p 849–856
  44. S. Kou, *Welding metallurgy*, 2nd ed. John Wiley & Sons, Hoboken, 2002, p 263–285

**Publisher's Note** Springer Nature remains neutral with regard to jurisdictional claims in published maps and institutional affiliations.

Springer Nature or its licensor (e.g. a society or other partner) holds exclusive rights to this article under a publishing agreement with the author(s) or other rightsholder(s); author self-archiving of the accepted manuscript version of this article is solely governed by the terms of such publishing agreement and applicable law.